ELSEVIER

Contents lists available at ScienceDirect

Journal of Power Sources

journal homepage: www.elsevier.com/locate/jpowsour





Stabilizing cathode-electrolyte interphase of LiNi_{0.5}Mn_{1.5}O₄ high-voltage spinel by blending garnet solid electrolyte in lithium-ion batteries

Xinwei Jiao, Lalith Rao, Junwei Yap, Chan-Yeop Yu, Jung-Hyun Kim

Department of Mechanical and Aerospace Engineering, The Ohio State University, Columbus, OH, 43212, United States

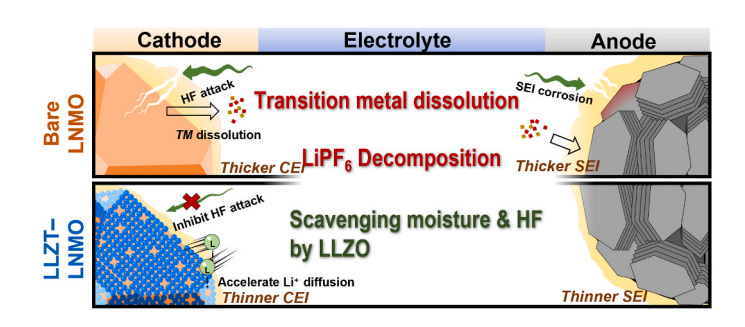
HIGHLIGHTS

- LLZT solid electrolyte (SE) as Li⁺ conducting and HF scavenging additive for LNMO.
- 5 wt% LLZT blended LNMO cathode delivered an optimal electrochemical performances.
- SEI and CEI became more stable during high-voltage cycles by adding 5 wt% LLZT.
- SE blending is cost-effective, and manufacturing friendly vs. conventional coating.

ARTICLE INFO

Keywords:
High-voltage cathodes
Garnet solid electrolyte
LNMO spinel
Blended cathode
Li-ion batteries

GRAPHICAL ABSTRACT



ABSTRACT

This work presents a strategy of blending $\text{Li}_{6.7}\text{La}_3\text{Zr}_{1.7}\text{Ta}_{0.3}\text{O}_{12}$ (LLZT) garnet solid electrolyte into $\text{LiNi}_{0.5}\text{Mn}_{1.5}\text{O}_4$ (LNMO) high-voltage spinel cathode to enhance electrochemical performances and stabilities of electrode/ electrolyte interphase layers in full-cells. Among a series of samples, 5 wt% LLZT blended LNMO delivered improved capacity, cycle life, and rate capability compared with a bare LNMO. The improvement mechanism of LLZT blended cathode can be explained in two folds. First, LLZT contacts with LNMO and improves Li^+ transport properties of the cathode-electrolyte interphase (CEI) layer, as evidenced by electrochemical impedance spectroscopy (EIS) and distribution of relaxation time (DRT) analyses. Second, LLZT can scavenge moisture/proton in the electrolyte, oxidative decomposition products from the electrolyte, and suppress the degradation of CEI and solid-electrolyte interphase (SEI) layers during extended cycles, as evidenced by X-ray photoelectron spectroscopy (XPS). As a result, the 5 wt% LLZT blended LNMO cathode delivered a stable electrochemical performance even in the presence of 5000 ppm moisture (and thus HF) in an electrolyte. In contrast to the traditional surface coating methods, the solid-electrolyte blending approach is cost-effective, manufacturing/environmentally friendly, and thereby can serve as a practical pathway for improving the performances and stability of current battery cells for EV and small electronics.

1. Introduction

The LiNi_{0.5}Mn_{1.5}O₄ (LNMO) spinel is an attractive cathode material

for lithium-ion batteries (LiBs) due to its low material cost and high operating voltage (e.g., >4.7 $V_{vsl.\ Li}$) [1,2]. Moreover, LNMO has a good rate capability attributed to its three-dimensional Li^+ diffusion

E-mail address: kim.6776@osu.edu (J.-H. Kim).

 $^{^{\}star}$ Corresponding author.

pathways in its lattice [3,4]. However, the LNMO/graphite full cells suffered from serious capacity fading. Current understanding of the degradation mechanisms of LNMO at high voltages includes (1) oxidative decomposition of liquid electrolytes and consequent degradation of cathode electrolyte interfaces (CEI), (2) transition metal (TM) dissolution and migration to the anode side, (3) consumption of ${\rm Li}^+$ through parasitic reactions at the solid electrolyte interface (SEI) at graphite anodes [2,4,5].

Recent studies have focused on coating the LNMO cathode by using a thin layer of metal oxide or metal phosphate to suppress parasitic reactions at the CEI layer. For example, it has been reported that V_2O_5 [6], Al_2O_3 [7], ZnO [8], and ZrP [9] coating on LNMO particles could protect the CEI from HF attack and consequently improve the LiB performances. In contrast, some of the coating materials had intrinsically poor Li^+ conductivity that unwantedly led to lower discharge capacity [10]. Therefore, Li-ion conducting solid electrolytes such as $\rm Li_7La_3Zr_2O_{12}$ (LLZO) and $\rm Li_{1.4}Al_{0.4}Ti_{1.6}(PO_4)_3$ (LATP) have been proposed as alternative coating materials [11–13].

Besides the coating materials, the coating method is another critical factor that governs the performance of cathode materials. Most common coating methods include wet chemical coating processes such as sol-gel, dry coating processes such as powder coating, physical/chemical vapor depositions such as atomic layer decomposition (ALD) technique [14]. The dry coating process is cost-efficient but has less control on coating thickness, morphology, and homogeneity [15]. These problems can be solved by using the wet chemical coating process at the expense of extra processing steps. For example, Belharouak et al. [15] discussed that the wet coating process requires extra cost due to the wastewater treatment and subsequent drying of the coated materials and can unwantedly modify the surface chemistry of cathodes by leaching lithium with solvents used for the coating process. Moreover, coating solid electrolytes on cathode powders by wet coating methods requires extra high-temperature calcination, which can cause the migration of the coating element into the lattice of LNMO [11]. Finally, physical/chemical vapor deposition of solid electrolyte materials onto LNMO particles will be challenging due to the complexity and high cost of the process.

In our previous work, we reported that blending $\text{Li}_{6.7}\text{La}_3\text{Zr}_{1.7}$. $\text{Ta}_{0.3}\text{O}_{12}$ (LLZT) garnet-type solid electrolyte with $\text{LiNi}_{0.6}\text{Mn}_{0.2}\text{Co}_{0.2}\text{O}_2$ (NMC622) cathode can effectively passivate the CEI and scavenge HF under its high-voltage operation (\sim 4.5 $\text{V}_{\text{vs.Li}}$) condition [16]. Due to the even higher operating voltage of LNMO cathodes (5.0 $\text{V}_{\text{vs.Li}}$ upper cut-off voltage), the parasitic reactions occurring at CEI will be accelerated further. Therefore, we adopted the LLZT blending strategy for the LNMO cathode and examined its effect on electrode-electrolyte interfacial stability and LNMO/graphite full-cell performances. Compared with the conventional surface coating methods, our proposed solid-electrolyte blending can offer advantages in terms of manufacturing friendliness, energy-saving, and cost-effectiveness, which can be a practical alternative to conventional coating for high-energy and high-voltage cathode materials in LiBs.

2. Experimental setup and characterization

2.1. Preparation of electrodes and battery cells

The LiNi_{0.5}Mn_{1.5}O₄ (LNMO) cathode active material (MSE supplies), conductive agent (Super-P), and polyvinylidene fluoride (PVdF) binder powders were mixed in 85:7.5:7.5 wt%. For LLZT-LNMO blending cathodes, LNMO powders were partly replaced by Li_{6.7}La₃Zr_{1.7}Ta_{0.3}O₁₂ (LLZT; Ampcera) powder with different ratios of 2.5 wt%, 5 wt%, and 10 wt%. Mesocarbon microbeads (MCMB) graphite was used as the anode for full cells, consisting of 89 wt% of active material, 4 wt% Super-P, and 7 wt% PVdF binder. Each electrode material was thoroughly mixed with *N*-methyl-2-pyrrolidone (NMP, Alfa Aesar) solvent and a zirconia bead to form a slurry by using a planetary mixer (Thinky).

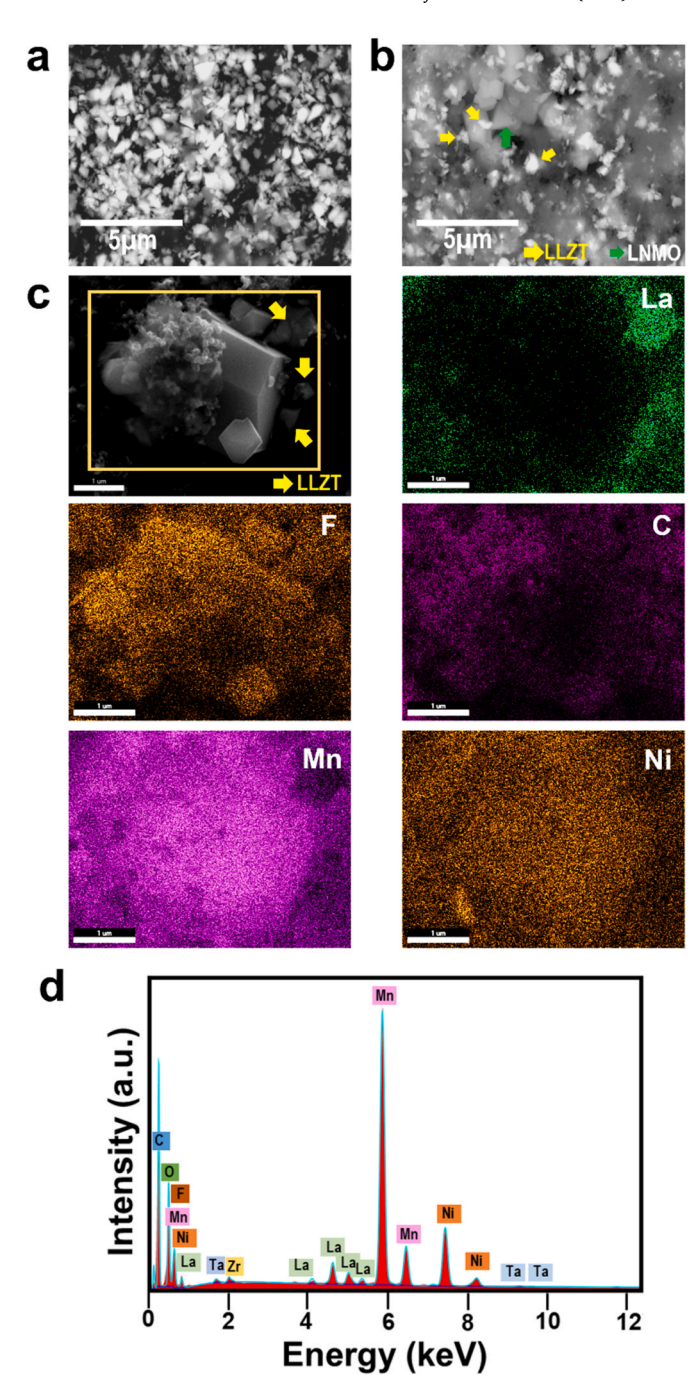


Fig. 1. (a) SEM image of LLZT powder. (b)–(d) SEM, elemental mapping, and EDS spectrum images of 5 wt% LLZT-LNMO cathode.

The obtained slurry was homogeneously spread on the Al current collector for cathodes and dried in an oven overnight at 80 $^{\circ}\text{C}.$ Li-ion batteries were fabricated as CR2032 coin-type half-cells (using Li metal anode) and full-cells (using graphite anode) by using 1 M LiPF₆ in ethylene carbonate (EC): ethyl methyl carbonate (EMC) solvents (1:1 wt ratio) and a piece of separator (Celgard 2500). A moisture-contaminated electrolyte was prepared by adding 50 μL deionized water to 10 mL liquid electrolyte.

2.2. Electrochemical and physical characterizations

The assembled half- and full-cells were, respectively, tested in a voltage range of 3.5–5.0 V and 3.4–4.9 V by using a battery cycling station (Arbin LBT System) in an environmental chamber (at 25 $^{\circ}$ C).

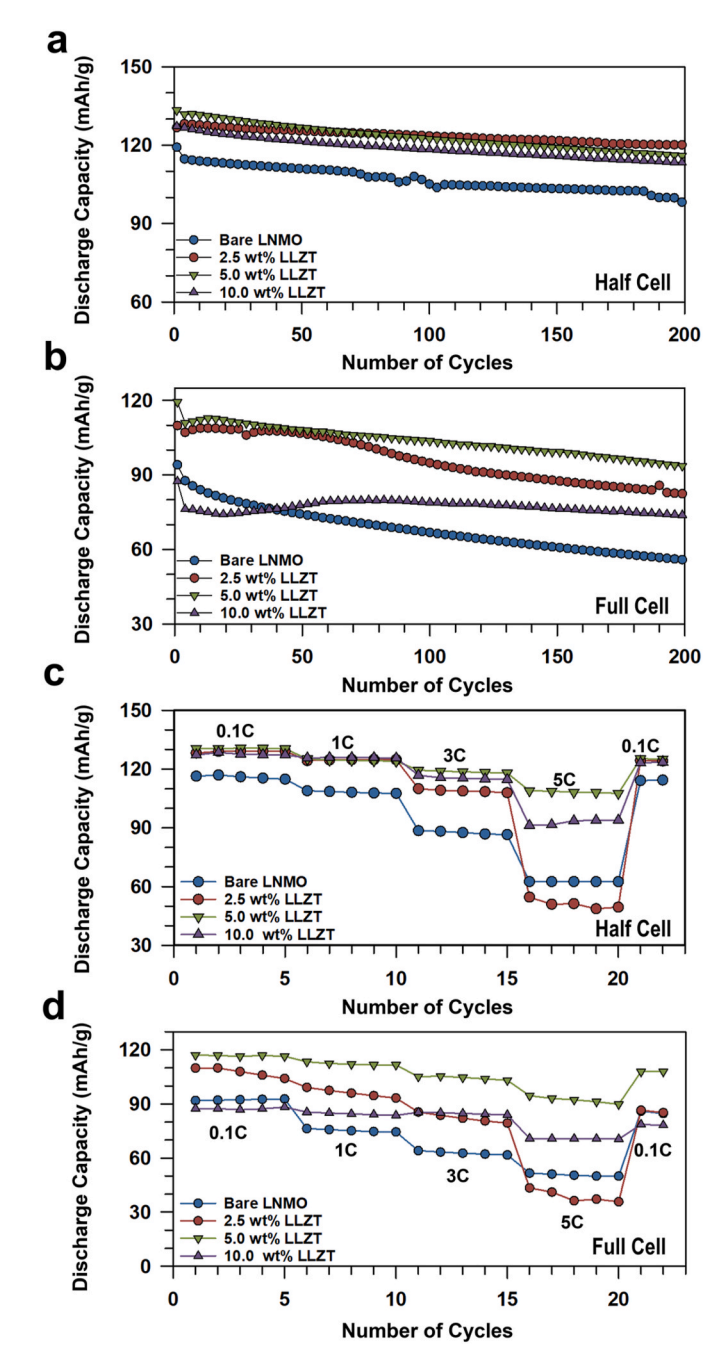


Fig. 2. Cycle life and rate capability of (a,c) half-cells and (b,d) full-cells made with the LLZT-LNMO blended cathodes having various LLZT contents in a range of 0–10 wt%. The half-cells and full-cells were, respectively, cycled in voltage ranges of 3.5–5.0 $V_{\rm vs.Li}$ and 3.4–4.9 V at 25 °C. For the rate-capability tests, the cells were charged at a constant C/10-rate and discharged at various C-rates.

Electrochemical impedance spectroscopy (EIS) was measured using a potentiostat (Grammy Interface 1010E). The Nyquist plots were further analyzed by distribution of relaxation time (DRT) technique [17].

The scanning electron microscope (SEM, FEI Apreo LoVac) with energy-dispersive X-ray spectroscopy (EDS) was performed on fresh and cycle-aged electrodes. After cycling tests, full-cells were disassembled in an Ar-filled glovebox to recover cycle-aged electrodes, followed by washing in dimethyl carbonate for 2 min. X-ray photoelectron spectroscopy (XPS, Kratos AXIS with Mg K α source) analysis was performed on the cycled cathodes. To minimize surface charging, charge neutralization was enabled, and spectra were calibrated based on C–C peaks at 284.7 eV. The resulting spectra were fit using CasaXPS software.

3. Results and discussion

Fig. 1a shows that the pristine LLZT powder consists of ~500 nm particles. The electrode morphology and distribution of 5 wt% LLZT solid electrolyte in LNMO (hereafter noted as 5 wt% LLZT-LNMO) were observed using SEM and EDS. Fig. 1b shows a good dispersion of LLZT (brighter particle due to its higher molecular weight) witin 3-6 µm LNMO particles in the 5 wt% LLZT-LNMO cathode. EDS spectrum of the LLZT (5 wt%) - LNMO blended cathode shows the composition of Ni: 2.04 at%, Mn: 7.15 at%, C: 63.20 at%, O: 19.91 at%, F: 7.09 at%, La: 0.38 at%, Ta: 0.07 at%, and Zr: 0.15 at%, respectively. The elemental mapping image in Fig. 1c shows that \sim 3 µm LNMO particle is contacting with sub-micron-sized LLZT solid-electrolyte particles in the cathode. The contents of Mn, Ni, and La were determined to be 21.77 wt%, 6.65 wt%, and 2.93 wt%, respectively. This corresponds to an average TM/La ratio of ~29.10, which is close to the target ratio of 24.8 in the 5 wt% LLZT-LNMO. This result demonstrates the homogenous distribution of LLZT within the LNMO cathode. Further increase in LLZT contents led to its local agglomeration, as shown from the 10 wt% LLZT - LNMO cathode in Fig. S1.

In previous study, we reported that 5 wt% LLZT blending to LiNi_{0.6}Mn_{0.2}Co_{0.2}O₂ (NMC622) cathode was beneficial in terms of fullcell (i.e., NMC622/graphite) performances. The optimal content of LLZT within the LLZT-LNMO cathode needs to be identified for (i) balancing ionic and electronic transport properties of the blended cathodes and (ii) minimizing a loss of gravimetric energy density of cathode caused by adding inactive LLZT solid-electrolyte. Therefore, we first examined the effect of LLZT contents on the electrochemical properties of the LNMO - LLZT blended cathodes. Half-cell performances of the blended cathodes with the LLZT contents of 2.5, 5.0, and 10.0 wt% were compared with the bare LNMO cathode. Fig. S2 shows voltage profiles and corresponding dQ/dV profiles of the half-cells. All the cathodes have a plateau at around 4.7 $V_{Vs,Li}$ attributed to the Ni^{2+} / Ni^{4+} redox couple, and a short plateau in the $\sim 4V_{Vs,Li}$ region attributed to the Mn³⁺/Mn⁴⁺ redox [2]. There was no evidence that LLZT was involved in the electrochemical charge-discharge reaction. More importantly, the bare LNMO suffered from a significant increase in Ohmic voltage polarization ($\Delta V = \Delta I \bullet R$) during repeated cycling. In earlier study, we reported that parasitic reactions at CEI and SEI are responsible for such cell impedance growth during cycling [2,18]. Adding 2.5 wt% LLZT to LNMO (hereafter noted as 2.5 wt% LLZT-LNMO) suppressed the voltage polarization during 100 cycles. In stark contrast, the 5 wt% LLZT-LNMO cathode could maintain its initial voltage profiles without noticeable voltage polarization during cycling. Finally, adding 10 wt% LLZT to LNMO (hereafter noted as 10 wt% LLZT-LNMO) showed a slight increase in voltage polarization again, suggesting that 5 wt% LLZT addition will be optimal for stabilizing the CEI and SEI and suppressing the cell impedance growth.

Fig. 2a compares the cycle life of the half-cells. The bare LNMO delivered an initial discharge capacity of 119.19 mAh/g and 82.4% capacity retention after 200 cycles. In contrast, the 2.5 wt% LLZT-LNMO, 5 wt% LLZT-LNMO and 10 wt% LLZT-LNMO cathode, respectively, delivered higher initial discharge capacities of 132.3 mAh/g, 128.9 mAh/g, and 127.2 mAh/g. Here, it should be noted that the specific capacities of LLZT-LNMO cathodes (shown in Fig. 2a) were determined by considering LNMO's mass only, and the LLZT's mass would decrease the electrode-level capacities. The LLZT-LNMO blended cathodes delivered improved capacity retentions in a range of 86.3–88% comparing with the bare LNMO cathode.

Fig. 2b compares the capacity retentions of full-cells when cycled in a range of 3.4–4.9 V at 25 °C. The initial discharge capacity of a full-cell made with the bare LNMO cathode is 94.1 mAh/g, and its capacity retentions after 200 cycles is 59%. Comparing with the LNMO/Li half-cell, the LNMO/graphite full-cell suffers from poor capacity retention during cycling. We reported that the series of parasitic reactions at both cathode and anode sides are the main source of the degradation [19–21]. An

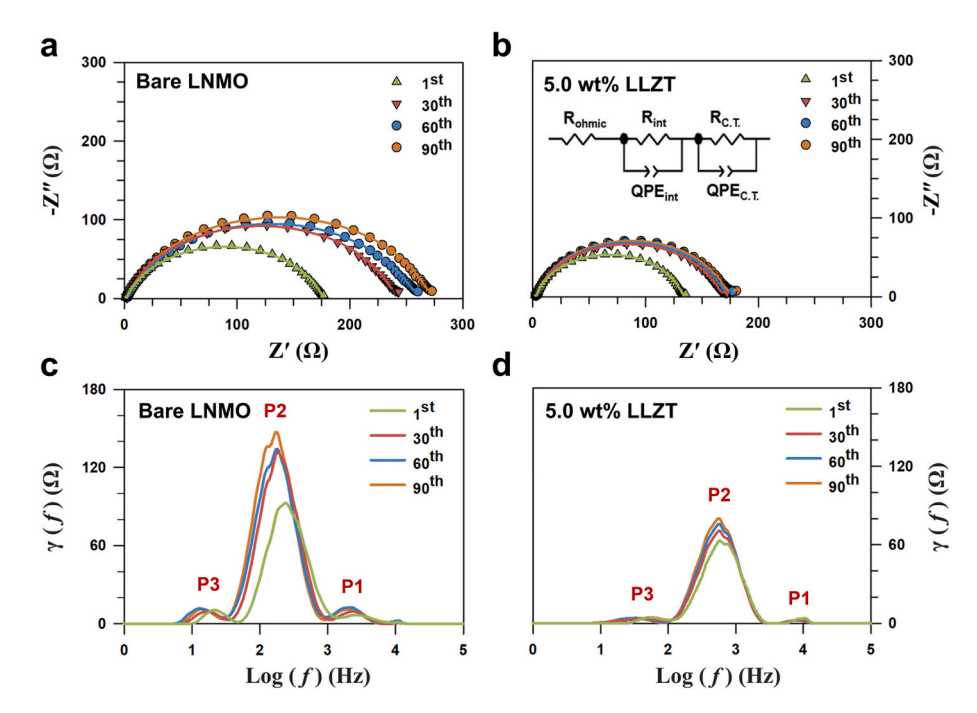


Fig. 3. Nyquist plots of half-cells made with (a) bare LNMO and (b) 5 wt% LLZT-LNMO cathodes. The data were collected at 50% state-of-charge (SOC) during cycling at 25 °C. Experimental data (symbols) was fitted (black lines) with the electrical circuit model shown in Fig. 3b. DRT data analyzed from the corresponding Nyquist plots of (c) bare LNMO and (d) 5 wt% LLZT-LNMO cathodes.

electrolyte oxidation produces HF and leads to transition metal dissolution (e.g., $\mathrm{Mn^{2+}}$), which in turn migrates and continuously catalyze SEI regeneration at the expense of active $\mathrm{Li^{+}}$ [20,21]. In addition, the resulting thick graphtie SEI and LNMO CEI can increase the internal reistance of cells, underming the $\mathrm{Li^{+}}$ diffusion kinetics at the electrolyte-electrode interfaces [18]. Such the poor cycle life of the LNMO full-cells has become the most critical barrier of its commercialization.

In contrast, full-cells made with the LLZT-blended LNMO cathodes delivered enhanced specific capacities and cycling performances comparing with the bare LNMO cathode. For example, the 2.5 wt%, 5 wt %, 10 wt% LLZT blended LNMO cathodes, respectively, delivered initial discharge capacities of 109.8 mAh/g, 119.3 mAh/g, and 87.4 mAh/g, and capacity retention values of 74.94%, 78.27%, and 84.35%, after 200 cycles. Among the samples, the 5 wt% LLZT-LNMO showed the highest capacities of 93.4 mAh/g after 200 cycles, which is $\sim\!68.3\%$ improvement over the bare LNMO cathode. The different initial discharge capacities in the LLZT blending electrodes can be attributed to the properties of the solid-state electrolyte. For the 10 wt% LLZT – LNMO cathode, the local agglomeration of LLZT particles would impede electron conduction pathways between LNMO particles (see, Fig. S1). This may explain the lower specific capacity of LLZT although it offered the best capacity retentions among the samples.

To further investigate the effect of LLZT blending on rate capabilities of the half-cells and full-cells, all the cells were charged at a constant rate of C/10 followed by discharging at different C-rates of 0.1, 1.0, 3.0 and 5.0 for 5 cycles, respectively. Fig. 2c shows that the 5 wt% LLZT-LNMO half-cell delivers the best rate performance among all the cells. Even at the 5 C-rate discharging, the 5 wt% LLZT-LNMO delivered 108.9 mAh/g (~82.45% capacity retention) while the bare LNMO delivered 63.4 mAh/g. The 5 wt% LLZT-LNMO cathode still exhibits the best rate capability in full-cells, as shown in Fig. 2d. The rate capability of a cathodes is highly dependent on the transport properties (both Li $^+$ and e $^-$) between the two electrodes. The results demonstrate that 5 wt% LLZT-LNMO cathode offers the optimal transport behavior of both Li $^+$ and e $^-$ among the series of samples. Further increase in LLZO content can improve the cycle life at the expense of specific capacity but reduce

cell-level energy density. The inferior rate-capability of 2.5 wt% LLZT-LNMO cathode suggests that 2.5 wt% LLZT is not enough to provide enough Li⁺ conductivity or passivate CEI while impeding electronic conductivity, which agrees well with our prior report on LLZT-NMC blended cathodes [16].

The electrochemical impedance spectroscopy (EIS) of bare LNMO and 5 wt% LLZT-LNMO half-cells were collected at every 30 cycles at their 50% state-of-charge (SOC). During the analysis, a contribution of Li SEI on half-cell impedance can be assumed to be identical because the Li metal in half-cell experienced the same electrochemical history [13]. This would allow comparing the impedance behaviors of the working electrode. Fig. 3a and b respectively show their Nyquist plots which were fitted with an electrochemical circuit model (ECM) as shown in Fig. 3b. The intercept at the high-frequency region is ohmic resistance ($R_{\rm ohmic}$), which mainly correspond to an electrolyte resistance; the high to middle-frequency arc is associated with interface resistances ($R_{\rm int}$) from both CEI and Li SEI; the low-frequency arc, which is merged with the higher frequency arc, is associated with a charge transfer resistance ($R_{\rm CT}$) [22].

Although the Nyquist plots sufficiently demonstrate the difference in impedance amplitude and growth between the two samples, they lack resolution in deconvoluting individual impedance sources. Therefore, the distribution of relaxation time (DRT) analysis was utilized in this study, and the corresponding results are shown in Fig. 3c and d. The resulting DRT plots present three major sources of electrochemical impedance from the bare LNMO and 5 wt% LLZT-LNMO cathodes: P1 (10³–10⁴ Hz) for contact impedance between particles or between materials and current collectors, P2 (10²-10³ Hz) originating from CEI and SEI, and P3 (10^1-10^2 Hz) for charge transfer [23-26]. The DRT data from the bare LNMO cathode shows that the increase in CEI impedance is responsible for the overall cell impedance growth during cycling. In contrast, the 5 wt% LLZT-LNMO cathode has stable CEI impedance values during the cycling, suggesting that LLZT has a positive effect on maintaining a good Li⁺ transport properties of the CEI, which agrees well with our prior report on LLZT-NMC blended cathodes [16].

To understand the difference in CEI properties between the bare LNMO and the 5 wt% LLZT-LNMO cathodes, we measured XPS of cycle-

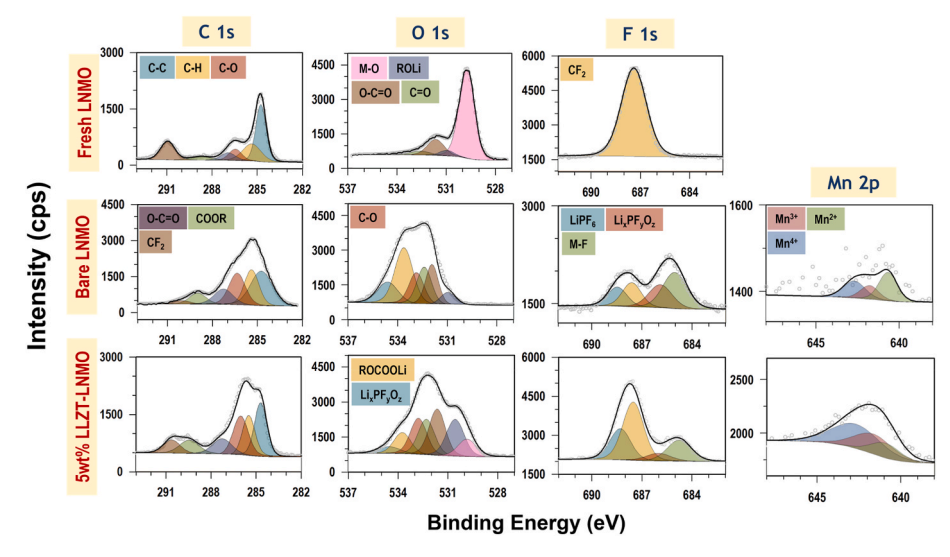


Fig. 4. XPS spectra for representative surface elements from CEI layers of (i) fresh, bare LNMO, (ii) cycle-aged bare LNMO, and (iii) cycle-aged 5 wt% LLZT-LNMO cathodes. The cycle-aged cathodes were recovered from the full-cells after 200 cycles, of which performances were demonstrated in Fig. 2b.

aged cathodes. Here, the cycled cathodes were recovered from 200-times cycled full-cells, of which performances were demonstrated in Fig. 2b. Fig. 4 plots their C 1s, O 1s, F 1s, and Mn 2p XPS spectra in comparison to the fresh LNMO cathode. The C 1s spectrum of the fresh LNMO cathode retains relatively high C–C (~284.7 eV) and C–H (~285.3 eV) peak intensities from conductive carbon black and PVdF binder, respectively. After 200 cycles in full-cells, XPS data from the bare LNMO and 5 wt% LLZT-LNMO cathodes exhibit presences of lithium alkoxides (ROLi), lithium carbonate (Li₂CO₃), metal fluorides (MF₂), and alkyl carbonate (ROCOOLi) in their CEIs, which agrees very well with literature [27,28]. The resulting XPS spectra from different elements consistently indicates that the 5 wt% LLZT – LNMO has thinner CEI layer than that of the bare LNMO after 200 cycles. For example, the.

M-O peaks (at ~529.8 eV) in O 1s spectra is from the LNMO and thus has the highest intensity for the fresh LNMO. After 200 cycles, absence of the M-O peak from the bare LNMO can be explained by a thick SEI deposition onto the cycle-aged LNMO. In contrast, the 5 wt% LLZT-LNMO still retains the M-O peak, indicating its thinner CEI than that of the bare LNMO. In addition, the relative intensity of the C–C peak

to the C–O peaks reflects the thickness of the CEI layer [19,22,29]. The peak ratio of C–C to C–O were, respectively, 1.15 for the bare LNMO and 1.27 for the 5 wt% LLZT-LNMO. Its relatively high ratio (i.e., 1.27) also confirms that the 5 wt% LLZT – LNMO cathode has thinner CEI layer than the bare LNMO cathode.

In the F 1s spectra, the peaks at 684.8 eV and 686.4 eV, respectively, can be assigned to M-F and $Li_xPF_yO_z.$ At high-voltage cell operation (e. g., $>\!4.3~V_{vs,Li})$, the reaction between residual moisture and LiPF $_6$ is accelerated because PF_6^- lowers the oxidation threshold of H_2O and decreases the energy barrier of the hydrolysis reaction, producing a larger amount of HF and $Li_xPF_yO_z$ of which reaction mechanisms are listed below [30].

$$LiPF_6 \rightleftharpoons PF_5 + LiF$$
 [1]

$$PF_5 + H_2O \rightarrow POF_3 + 2HF$$
 [2]

$$POF_3 + Li^+ \rightarrow Li_x PF_y O_z + LiF$$
 [3]

When we compare the F 1s spectra of both cycled cathodes, amounts

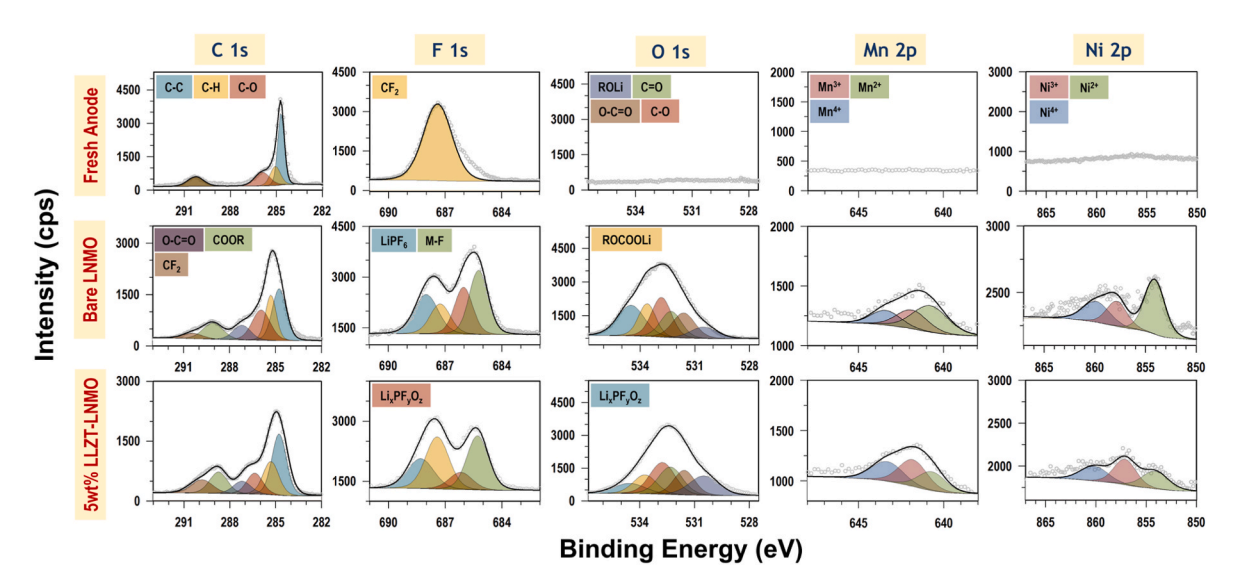


Fig. 5. XPS spectra for representative surface elements from SEI layer on (a) fresh graphite anode, (b) cycle-aged graphite anode paired with the bare LNMO in full-cells, and (c) cycle-aged graphite anode paired with the 5 wt% LLZT-LNMO cathodes in full-cells. The cycle-aged anodes were recovered from the full-cells after 200 cycles, of which performances were demonstrated in Fig. 2b.

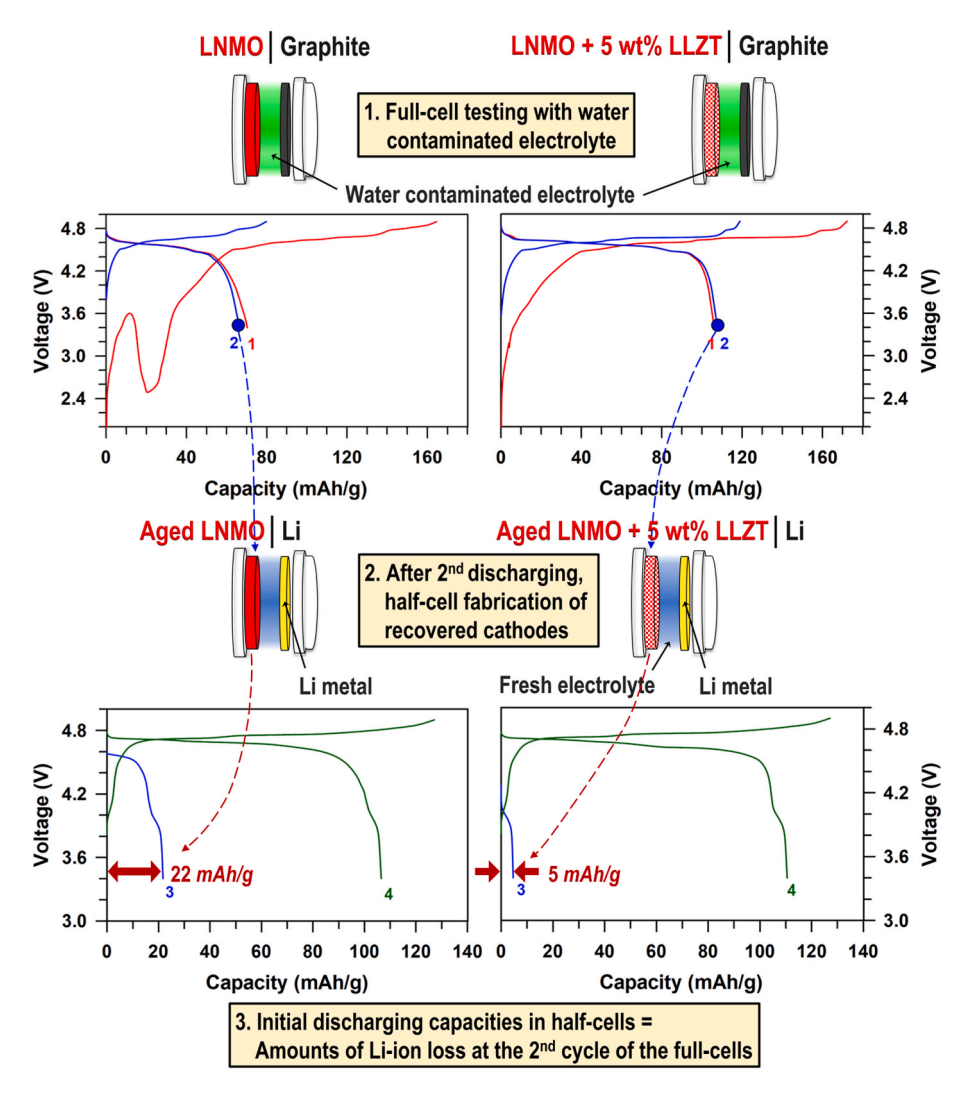


Fig. 6. Experimental process that was designed to identify the impact of 5 wt% LLZT in blended cathode on suppressing parasitic reactions and consequent active Li⁺ loss from the moisture/proton-attack in full-cell.

of M - F and Li $_x$ PF $_y$ O $_z$ of the 5 wt% LLZT–LNMO are significantly lower than the bare LNMO, which agrees well with our previous result obtained from the LLZT blended NMC cathodes [16]. In the Mn $2p_{1/2}$ spectra, the different ratios of Mn $^{2+}$ (at $\sim\!640.9$ eV), Mn $^{3+}$ (at $\sim\!641.7$ eV), and Mn $^{4+}$ (at $\sim\!642.7$ eV) [31,32] were observed between the two cycled cathodes. Compared with the bare LNMO, the 5 wt% LLZT–LNMO shows a relatively low peak intensity of Mn $^{2+}$. The Mn $^{2+}$ at the surface of LNMO was associated with the presence of MnF $_2$, which was re-deposition product of the dissolved Mn $^{2+}$ after the HF attack [21]. The low Mn $^{2+}$ peak intensity of the 5 wt% LLZT–LNMO can be explained by proton scavenging of LLZT and thereby less severe Mn $^{2+}$ dissolution.

We also performed XPS analysis of SEI layers on graphite anodes after 200 cycles in full-cells (see, Fig. 2c), which were paired with the bare LNMO or the 5 wt% LLZT-LNMO cathodes. The representative XPS spectra are plotted in Fig. 5. For the C 1s spectra, the graphite anodes paired with the bare LNMO and 5 wt% LLZT-LNMO, respectively, have C–C/C–O peak ratios of 1.01 and 1.86. The result suggests that employing the 5 wt% LLZT-LNMO cathode contributes to maintain the tinner SEI thickness on graphite. This assumption is supported by the reduced intensities of M – F (LiF, MnF₂, and NiF₂) peaks (see, F 1s, Mn 2p, and Ni 2p spectra) and Li_xPF_yO_z peaks (see, F 1s and O 1s spectra) from the graphite SEI paired with the 5 wt% LLZT-LNMO cathode. The existence of Mn and Ni species with oxidation states of +2 or higher on

cycled graphite SEI is consistent with literatures [33,34].

Our earlier report presented that electrolyte oxidation and production of HF acid is responsible for the TM dissolutions, which tends to be accelerated by time, temperature, and cell voltage [21]. The dissolved Ni^{2+} and Mn^{2+} ions from LNMO can migrate to and damage the graphite SEI layer during their re-deposition into metallic clusters or metal fluorides [35,36]. Such damaged SEI layer undergoes a self-healing process at the expense of active Li-ion and electrolyte solvents [20, 37]. Therefore, more severe parasitic reactions occurring at CEI leads to a thicker SEI layer production on graphite anode, which in turn reduces the capacity (by losing cyclable Li-ions) and increases a cell impedance.

The XPS analysis of cycled electrodes demonstrated that LLZT addition to LNMO could effectively suppress the parasitic reactions and maintain relatively thinner CEI and SEI layers. More importantly, the 5 wt% LLZT-LNMO full-cell exhibited low peak intensities of $\rm Li_x PF_y O_z$ and LiPF₆ from both cathode and anode surfaces comparing with the bare LNMO. Sharafi et al. [33] has reported that the $\rm Li_7 La_3 Zr_2 O_{12}$ (LLZO) garnet solid electrolyte is moisture sensitive and can consume the residual water by scavenging protons by following reaction routes:

$$\text{Li}_7\text{La}_3\text{Zr}_2\text{O}_{12} + x\text{H}_2\text{O} \rightarrow \text{Li}_{7-x}\text{H}_x\text{La}_3\text{Zr}_2\text{O}_{12} + x\text{LiOH}$$
 [4]

$$\text{Li}_{7}\text{La}_{3}\text{Zr}_{2}\text{O}_{12} + x\text{H}_{2}\text{O} \rightarrow \text{Li}_{7-2x}\text{H}_{2x}\text{La}_{3}\text{Zr}_{2}\text{O}_{12} + x\text{Li}_{2}\text{O}$$
 [5]

Therefore, it can be inferred that LLZT can scavenge the moisture in

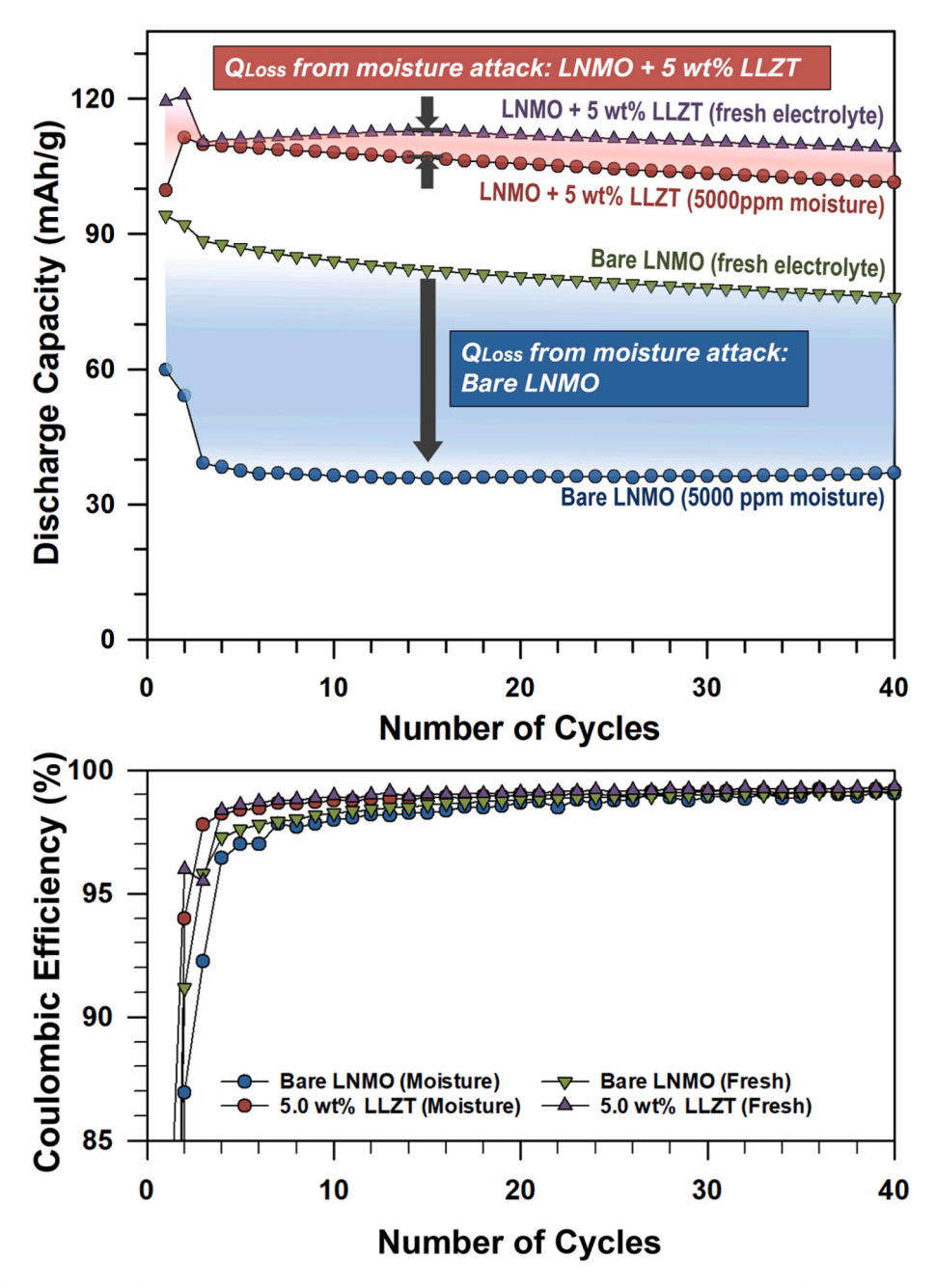


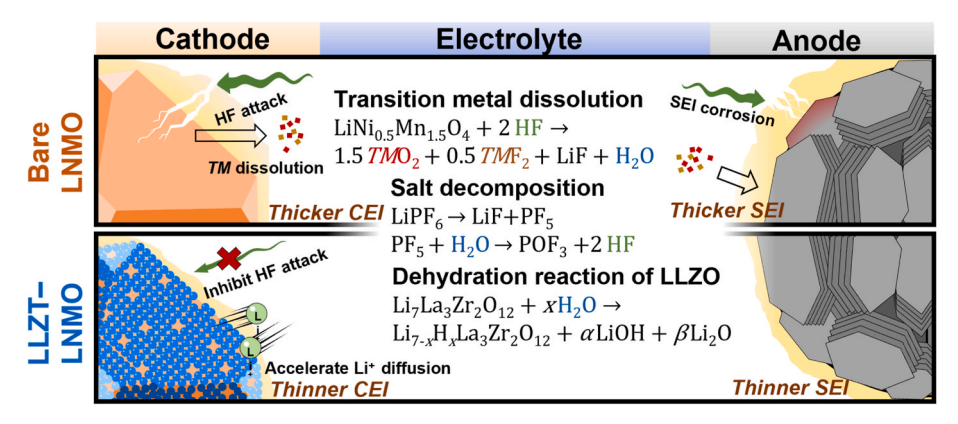
Fig. 7. Comparison of full-cells (a) cycle lives and (b) Coulombic efficiencies of bare LNMO and 5 wt% LLZT-LNMO cathodes by using fresh electrolyte and moisture-contaminated (5000 ppm) electrolytes. The degrees of capacity losses (Q_{Loss}) from the moisture attacks was compared each other. All the full-cells were cycled at C/10 for two formation cycles and C/3 for rest of cycles in a voltage range of 3.4–4.9 $V_{vs.Li}$ at 25 °C.

the liquid electrolyte and suppress the parasitic reactions.

To prove this assumption, we designed series of experiments as shown in Fig. 6. Considering that high concentration of $\rm H_2O$ accelerates the oxidative decomposition of LiPF₆ and produces more HF [30], first, 5000 ppm (by mass) deionized water was mixed with a commercial electrolyte as a moisture-contaminated electrolyte to emphasize the effect of the LLZT additive on preventing the moisture attack. Then, bare LNMO and 5 wt% LLZT-LNMO cathodes, respectively, were fabricated into full-cells using the moisture contaminated electrolyte. The full-cell made with the bare LNMO cathode experienced severe voltage fluctuation during an initial charging due to moisture-related decomposition reaction, followed by a noticeable discharge capacity loss. For example, the discharge capacity after 2 cycles was 66 mAh/g, experiencing 28% capacity loss from the full-cell made with a fresh electrolyte (e.g., 92 mAh/g in Fig. 2c). In contrast, another full-cell made with the 5 wt%

LLZT-LNMO cathode delivered a discharge capacity of 108 mAh/g after 2 cycles with normal voltage profiles, which corresponds to 10% capacity loss from the full-cell made with the fresh electrolyte (e.g., 118 mAh/g in Fig. 2c). The severe irreversible charging process of bare LNMO is indicative of inevitable parasitic reactions at electrode-electrolyte interfaces in the presence of moisture in electrolyte, which accompanies with massive Li $^{\rm h}$ loss and impedance growth of CEI and SEI layers due to increases in surface byproducts such as Li $_{\rm x}$ P- $_{\rm y}$ O $_{\rm z}$ and LiF [34].

After 2nd discharging of full-cells made with the moisture-contaminated electrolyte, each cathode was recovered and refabricated into half-cell using a fresh electrolyte and Li-metal as an anode. The schematic of this experiment is shown in Fig. 6. The amount of Li-loss from each cathode after the 2 cycles is equivalent to its initial discharge capacity of the half-cell. As a result, the bare LNMO cathode



 $\textbf{Scheme 1.} \ \ \text{Degradation reaction mechanisms of LiPF}_6 \ \ \text{at high voltages and positive roles of LLZT solid electrolyte on passivating CEI and SEI layers of LNMO cathode. } \\$

lost significant Li-ions corresponding to \sim 22 mAh/g due to the moisture attack. In contrast, the 5 wt% LLZT-LNMO cathodes only lost a small amount of Li-ions corresponding to \sim 5 mAh/g. After compensating the Li-loss, the half-cells delivered 2nd discharge capacities of 106 mAh/g for the bare LNMO cathode and 110 mAh/g for the 5 wt% LLZT-LNMO cathode, respectively.

The excess amount of HF in the electrolyte can expedite the corrosion of electrodes dissolution of TM ions (e.g., Mn^{2+} and Ni^{2+}) from LNMO that can migrate to graphite anode during the 1st charging (i.e., formation cycle). The dissolved Mn^{2+} and Ni^{2+} redeposit onto graphite surface with their reduced forms, which perturb the formation of graphite SEI layer and subsequently consume excessive amount of Liions (~22 mAh/g) during the formation cycle (i.e., initial 2 cycles) of the full cell (see, Fig. 6) [20,35]. On the other hand, LLZT in the 5 wt% LLZT-LNMO cathode could scavenge protons, and thereby suppresses the TM dissolution and consequent SEI degradation, as evidenced by its small amount of Li-loss (~5 mAh/g) during the formation cycles.

Fig. 7 compares cycle life of full-cells made with fresh and the moisture-contaminated electrolytes. Their voltage profiles are also compared in Fig. S3. The detrimental effect of the moisture in terms of specific capacities were observed immediately from the beginning of the cycles. The high moisture content (e.g., 5000 ppm) accelerates LiPF₆ decompositions following the reaction routes (1)-(3) and leads to thicker SEI and/or CEI layers deposited onto cycle-aged electrodes, as evidenced by their XPS spectra as shown in Fig. S4. After 40 cycles, the 5 wt% LLZT-LNMO cathode has higher C-C/C-O intensity ratio than that of the bare LNMO (see, Fig. S4). Besides, the low intensity of Li_xPF_vO_z peak and obvious M - O peak in the O 1s spectra from the 5 wt% LLZT-LNMO also suggest that LLZT contributed to suppress parasitic reactions involving the HF and maintained a thin CEI layer despite the highconcentration (5000 ppm) moisture attack. As a result, the 5 wt% LLZT-LNMO cathode could maintain good full-cell performances; (i) 91.7% capacity retentions (see, Fig. 7a) and (ii) normal voltage profiles (see, Fig. S3d) similar to the fresh-electrolyte cell during 40 cycles.

In contrast, the bare LNMO cathode suffered from severe voltage and capacity drops (see, Fig. 7 and S3c) due to the moisture attack. The thicker CEI formation on the bare LNMO cathode as confirmed by the XPS data (see, Fig. S4) not only consumed extra Li $^+$ corresponding to \sim 22 mAh/g (at the 2nd cycle, see Fig. 6) but could increase cell impedances. The bare LNMO cathode lost 55.7% of full-cell capacity during 40 cycles by using the moisture-contaminated electrolyte.

Coulombic efficiencies (CE) of the full-cells also decrease by using the moisture contaminated electrolyte, as shown in Fig. 7b. Their low CE values (e.g., 39% for the bare LNMO and 47% for the 5 wt% LLZT-LNMO) at the 1st cycles are indicative of severe parasitic reactions occurring at SEI and CEI during the 1st charging process (i.e., the formation cycle). During the long-term cycles, the full-cells delivered high CE values in order of 5 wt% LLZT-LNMO (fresh electrolyte) > 5 wt%

LLZT-LNMO (moisture-contaminated electrolyte) > bare LNMO (fresh electrolyte) > bare LNMO (moisture-contaminated electrolyte). By comparing the fresh and moisture-contaminated electrolytes, consistently low CE values from the moisture-contaminated electrolytes suggest that HF and $\rm H_2O$ continuously degraded the CEI and SEI layers in the full-cells during the extended cycles. By comparing the bare LNMO and the 5 wt% LLZT-LNMO cathodes, the LLZT acts as a proton and moisture scavenger and continuously improves the CEI stability in contact with both the fresh and the moisture-contaminated electrolyte.

4. Conclusion

In this study, we reported the strategy of blending LLZT garnet solid electrolyte into the LNMO spinel cathode to stabilize electrode/electrolyte interphase layers and improve the full-cell performances. Among the series of LLZT blended cathodes, the 5 wt% LLZT-LNMO delivered optimal performances in terms of specific capacity, capacity retention, and rate capability. The improvement mechanism of LLZT blended cathode can be explained by two folds. First, the LLZT contacts with LNMO active material and improves Li⁺ transport at the CEI layer, as evidenced by EIS and DRT analyses. Second, the LLZT can scavenge moisture/proton in the electrolyte, side reaction product from anodic decomposition of electrolyte, and suppress the degradation of CEI and SEI during the extended cycles, as evidenced by XPS and set of experiments with moisture-contaminated electrolyte. Scheme 1 illustrates the proposed improvement mechanisms of the LLZT-LNMO blended cathodes in full-cells. In contrast to the traditional surface coating methods, this solid-electrolyte blending approach is cost-effective and manufacturing/environmentally friendly, and thereby can serve as a practical pathway for improving performances and stability of current battery cells for EV and small electronics.

CRediT author statement

Xinwei Jiao: Conceptualization, Validation, Writing - Original Draft. Lalith Rao: Investigation, Data Curation. Junwei Yap: Investigation, Data Curation. Chan-Yeop Yu: Methodology, Visualization. Jung-Hyun Kim: Conceptualization, Writing - Review & Editing, Supervision.

Declaration of competing interest

The authors declare that they have no known competing financial interests or personal relationships that could have appeared to influence the work reported in this paper.

Data availability

Data will be made available on request.

Acknowledgments

Characterization of this work was supported in part by The Ohio State University Institute for Materials Research.

Appendix A. Supplementary data

Supplementary data to this article can be found online at https://doi. org/10.1016/j.jpowsour.2023.232748.

References

- [1] B. Aktekin, R. Younesi, W. Zipprich, C. Tengstedt, D. Brandell, K. Edström, The effect of the fluoroethylene carbonate additive in LiNi 0.5 Mn 1.5 O 4 Li 4 Ti 5 O 12 lithium-ion cells, J. Electrochem. Soc. 164 (2017) A942, https://doi.org/10.1149/2.0231706jes. –A948.
- [2] J.-H. Kim, N.P.W. Pieczonka, P. Lu, Z. Liu, R. Qiao, W. Yang, M.M. Tessema, Y.-K. Sun, B.R. Powell, In situ formation of a cathode-electrolyte interface with enhanced stability by titanium substitution for high voltage spinel lithium-ion batteries, Adv. Mater. Interfac. 2 (2015), 1500109, https://doi.org/10.1002/ admi.201500109.
- [3] G. Liu, Y. Lu, H. Wan, W. Weng, L. Cai, Z. Li, X. Que, H. Liu, X. Yao, Passivation of the cathode–electrolyte interface for 5 V-class all-solid-state batteries, ACS Appl. Mater. Interfaces 12 (2020) 28083–28090, https://doi.org/10.1021/ acsami.0c03610.
- [4] G. Liang, V.K. Peterson, K.W. See, Z. Guo, W.K. Pang, Developing high-voltage spinel LiNi $_{0.5}$ Mn $_{1.5}$ O $_4$ cathodes for high-energy-density lithium-ion batteries: current achievements and future prospects, J. Mater. Chem. A. 8 (2020) 15373–15398, https://doi.org/10.1039/D0TA02812F.
- [5] J.-H. Kim, N.P.W. Pieczonka, L. Yang, Challenges and approaches for high-voltage spinel lithium-ion batteries, ChemPhysChem 15 (2014) 1940, https://doi.org/ 10.1002/cphc.201400052. –1954.
- [6] J. Wang, S. Yao, W. Lin, B. Wu, X. He, J. Li, J. Zhao, Improving the electrochemical properties of high-voltage lithium nickel manganese oxide by surface coating with vanadium oxides for lithium ion batteries, J. Power Sources 280 (2015) 114–124, https://doi.org/10.1016/j.jpowsour.2015.01.087.
- [7] X. Fang, M. Ge, J. Rong, Y. Che, N. Aroonyadet, X. Wang, Y. Liu, A. Zhang, C. Zhou, Ultrathin Surface Modification by Atomic Layer Deposition on High Voltage Cathode LiNio. 5Mn1. 504 for Lithium Ion Batteries, Energy Technology, 2013. http://onlinelibrary.wiley.com/doi/10.1002/ente.201300102/abstract. (Accessed 13 May 2014). accessed.
- [8] J.C. Arrebola, A. Caballero, L. Hernán, J. Morales, Re-examining the effect of ZnO on nanosized 5V LiNi
 sub> 0.5 Mn
 sub> 1.5 O
 sub> 4 spinel: an effective procedure for enhancing its rate capability at room and high temperatures,
 J. Power Sources 195 (2010) 4278–4284.
- [9] H. Hu, Q. Chen, Z. Chen, H. Chen, Zirconium phosphate wrapped LiMn 1.5 Ni 0.5 O 4 used in lithium ion batteries as high voltage cathode material, Appl. Surf. Sci. 316 (2014) 348–354, https://doi.org/10.1016/j.apsusc.2014.08.009.
- [10] Z.A. Qureshi, H.A. Tariq, R.A. Shakoor, R. Kahraman, S. AlQaradawi, Impact of coatings on the electrochemical performance of LiNi0.5Mn1.5O4 cathode materials: a focused review, Ceram. Int. 48 (2022) 7374–7392, https://doi.org/ 10.1016/j.ceramint.2021.12.118.
- [11] L. Li, R. Zhao, D. Pan, S. Yi, L. Gao, G. He, H. Zhao, C. Yu, Y. Bai, Constructing trifunctional modification for spinel LiNi0.5Mn1.5O4 via fast ion conductor, J. Power Sources 450 (2020), 227677, https://doi.org/10.1016/j.jpowsour.2019.227677.
- [12] L. Li, R. Zhao, T. Xu, D. Wang, D. Pan, K. Zhang, C. Yu, X. Lu, G. He, Y. Bai, Stabilizing a high-voltage LiNi 0.5 Mn 1.5 O 4 cathode towards all solid state batteries: a Li-Al-Ti-P-O solid electrolyte nano-shell with a host material, Nanoscale 11 (2019) 8967–8977, https://doi.org/10.1039/C9NR01655D.
- [13] W. Liu, Q. Shi, Q. Qu, T. Gao, G. Zhu, J. Shao, H. Zheng, Improved Li-ion diffusion and stability of a LiNi_{0.5} Mn_{1.5} O₄ cathode through in situ co-doping with dualmetal cations and incorporation of a superionic conductor, J. Mater. Chem. A. 5 (2017) 145–154. https://doi.org/10.1039/C6TA08891K.
- [14] M. Chaudhary, S. Tyagi, R.K. Gupta, B.P. Singh, R. Singhal, Surface modification of cathode materials for energy storage devices: a review, Surf. Coating. Technol. 412 (2021), 127009, https://doi.org/10.1016/j.surfcoat.2021.127009.
- [15] U. Nisar, N. Muralidharan, R. Essehli, R. Amin, I. Belharouak, Valuation of surface coatings in high-energy density lithium-ion battery cathode materials, Energy Storage Mater. 38 (2021) 309–328, https://doi.org/10.1016/j.ensm.2021.03.015.
- [16] C.-Y. Yu, X. Jiao, L. Rao, S.-B. Son, E. Lee, J.-H. Kim, Garnet solid electrolyte blended LiNi0.6Mn0.2Co0.2O2 as high-voltage stable cathodes for advanced lithium-ion batteries, Electrochem. Commun. (2022), 107286, https://doi.org/ 10.1016/j.elecom.2022.107286.

- [17] T.H. Wan, M. Saccoccio, C. Chen, F. Ciucci, Influence of the discretization methods on the distribution of relaxation times deconvolution: implementing radial basis functions with DRTtools, Electrochim. Acta 184 (2015) 483–499, https://doi.org/ 10.1016/j.electacta.2015.09.097.
- [18] N.P.W. Pieczonka, V. Borgel, B. Ziv, N. Leifer, V. Dargel, D. Aurbach, J.-H. Kim, Z. Liu, X. Huang, S.A. Krachkovskiy, G.R. Goward, I. Halalay, B.R. Powell, A. Manthiram, Lithium polyacrylate (LiPAA) as an advanced binder and a passivating agent for high-voltage Li-ion batteries, Adv. Energy Mater. 5 (2015), 1501008, https://doi.org/10.1002/aenm.201501008.
- [19] L. Rao, X. Jiao, C.-Y. Yu, A. Schmidt, C. O'Meara, J. Seidt, J.R. Sayre, Y.M. Khalifa, J.-H. Kim, Multifunctional composite binder for thick high-voltage cathodes in lithium-ion batteries, ACS Appl. Mater. Interfaces 14 (2022) 861–872, https://doi. org/10.1021/acsami.1c19554.
- [20] J.-H. Kim, N.P.W. Pieczonka, Z. Li, Y. Wu, S. Harris, B.R. Powell, Understanding the capacity fading mechanism in LiNi0.5Mn1.5O4/graphite Li-ion batteries, Electrochim. Acta 90 (2013) 556–562, https://doi.org/10.1016/j. electacta.2012.12.069.
- [21] N.P.W. Pieczonka, Z. Liu, P. Lu, K.L. Olson, J. Moote, B.R. Powell, J.-H. Kim, Understanding transition-metal dissolution behavior in LiNi _{0.5} Mn _{1.5} O ₄ highvoltage spinel for lithium ion batteries, J. Phys. Chem. C 117 (2013) 15947–15957, https://doi.org/10.1021/jp405158m.
- [22] H. Chen, C. Yin, H. Zhou, Solvent-controlled the morphology and electrochemical properties of LiNi0.5Mn1.5O4 derived from metal-organic frameworks, Ionics 27 (2021) 4995–5008, https://doi.org/10.1007/s11581-021-04269-6.
- [23] X. Chen, L. Li, M. Liu, T. Huang, A. Yu, Detection of lithium plating in lithium-ion batteries by distribution of relaxation times, J. Power Sources 496 (2021), 229867, https://doi.org/10.1016/j.jpowsour.2021.229867.
- [24] N.S. Luu, J.-M. Lim, C.G. Torres-Castanedo, K.-Y. Park, E. Moazzen, K. He, P. E. Meza, W. Li, J.R. Downing, X. Hu, V.P. Dravid, S.A. Barnett, M.J. Bedzyk, M. C. Hersam, Elucidating and mitigating high-voltage interfacial chemomechanical degradation of nickel-rich lithium-ion battery cathodes via conformal graphene coating, ACS Appl. Energy Mater. 4 (2021) 11069–11079, https://doi.org/10.1021/acsaem.1c01995.
- [25] B. Manikandan, V. Ramar, C. Yap, P. Balaya, Investigation of physico-chemical processes in lithium-ion batteries by deconvolution of electrochemical impedance spectra, J. Power Sources 361 (2017) 300–309, https://doi.org/10.1016/j. ipowsour.2017.07.006.
- [26] K. Pan, F. Zou, M. Canova, Y. Zhu, J.-H. Kim, Comprehensive electrochemical impedance spectroscopy study of Si-Based anodes using distribution of relaxation times analysis. J. Power Sources 479 (2020), 229083.
- [27] Z. Xiao, R. Wang, Y. Li, Y. Sun, S. Fan, K. Xiong, H. Zhang, Z. Qian, Electrochemical analysis for enhancing interface layer of spinel LiNio.5Mn1.504 using ptoluenesulfonyl isocyanate as electrolyte additive, Front. Chem. 7 (2019) 591, https://doi.org/10.3389/fchem.2019.00591.
- [28] Y. Qian, P. Niehoff, M. Börner, M. Grützke, X. Mönnighoff, P. Behrends, S. Nowak, M. Winter, F.M. Schappacher, Influence of electrolyte additives on the cathode electrolyte interphase (CEI) formation on LiNi1/3Mn1/3Co1/3O2 in half cells with Li metal counter electrode, J. Power Sources 329 (2016) 31–40, https://doi.org/10.1016/j.jpowsour.2016.08.023.
- [29] X. Zheng, W. Liu, Q. Qu, H. Zheng, Y. Huang, Bi-functions of titanium and lanthanum co-doping to enhance the electrochemical performance of spinel LiNi0.5Mn1.5O4 cathode, J. Materiomics 5 (2019) 156–163, https://doi.org/ 10.1016/i.jmat.2019.01.007.
- [30] M. Liu, J. Vatamanu, X. Chen, L. Xing, K. Xu, W. Li, Hydrolysis of LiPF 6-containing electrolyte at high voltage, ACS Energy Lett. 6 (2021) 2096, https://doi.org/ 10.1021/acsenergylett.1c00707. –2102.
- [31] C. Ianhez-Pereira, Y.J. Onofre, C.J. Magon, A. de G. Rodrigues, M.P.F. de Godoy, The interplay between Mn valence and the optical response of ZnMnO thin films, Appl. Phys. A 126 (2020) 337, https://doi.org/10.1007/s00339-020-03511-8.
- [32] Y. Cai, S.-Z. Huang, F.-S. She, J. Liu, R.-L. Zhang, Z.-H. Huang, F.-Y. Wang, H.-E. Wang, Facile synthesis of well-shaped spinel LiNi 0.5 Mn 1.5 O 4 nanoparticles as cathode materials for lithium ion batteries, RSC Adv. 6 (2016) 2785–2792, https://doi.org/10.1039/C5RA21723G.
- [33] A. Sharafi, S. Yu, M. Naguib, M. Lee, C. Ma, H.M. Meyer, J. Nanda, M. Chi, D. J. Siegel, J. Sakamoto, Impact of air exposure and surface chemistry on Li–Li $_7$ La $_3$ Zr $_2$ O $_{12}$ interfacial resistance, J. Mater. Chem. A. 5 (2017) 13475–13487, https://doi.org/10.1039/C7TA03162A.
- [34] J. Choi, L. Dong, C.-Y. Yu, C. O'Meara, E. Lee, J.-H. Kim, Relationship of chemical composition and moisture sensitivity in LiNi x Mn y Co1 – X – Y O2 for lithium-ion batteries, J. Electrochem. Energy Conv. Storage 18 (2021), 041009, https://doi. org/10.1115/1.4051208.
- [35] N.M. Asl, J.-H. Kim, N.P.W. Pieczonka, Z. Liu, Y. Kim, Multilayer electrolyte cell: a new tool for identifying electrochemical performances of high voltage cathode materials, Electrochem. Commun. 32 (2013) 1–4, https://doi.org/10.1016/j. elecom.2013.03.031.